

See discussions, stats, and author profiles for this publication at: <https://www.researchgate.net/publication/264227254>

Three-Dimensional Simulation of Bubble Formation Through a Microchannel T-Junction

ARTICLE *in* CHEMICAL ENGINEERING & TECHNOLOGY · DECEMBER 2013

Impact Factor: 2.44 · DOI: 10.1002/ceat.201300169

CITATION

1

READS

16

4 AUTHORS, INCLUDING:



Bin Chen

Xi'an Jiaotong University

70 PUBLICATIONS 178 CITATIONS

SEE PROFILE



Li Guojie

Xi'an Jiaotong University

4 PUBLICATIONS 1 CITATION

SEE PROFILE

Bin Chen
Fang Guo
Guojie Li
Peng Wang

Xi'an Jiaotong University, State
Key Laboratory of Multiphase
Flow in Power Engineering,
Xi'an, Shaanxi, China.

Research Article

Three-Dimensional Simulation of Bubble Formation Through a Microchannel T-Junction

Three-dimensional simulations of bubble formation in Newtonian and non-Newtonian fluids through a microchannel T-junction are conducted by the volume-of-fluid method. For Newtonian fluids, the critical capillary number Ca for the transition of the bubble breakup mechanism is dependent on the velocity ratio between the two phases and the microchannel dimension. For the power law fluid, the bubble diameter decreases and the generation frequency increases with higher viscosity parameter K and power law index n . For a Bingham fluid, the viscous force plays a more important role in microbubble formation. Due to the yield stress τ_y , a high-viscous region is developed in the central area of the channel and bubbles deform to a flat ellipsoid shape in this region. The bubble diameter and generation frequency are almost independent of K .

Keywords: Bubbles, Fluid dynamics, Microchannel, Non-Newtonian fluids, Volume-of-fluid method

Received: March 19, 2013; *revised:* July 27, 2013; *accepted:* August 26, 2013

DOI: 10.1002/ceat.201300169

1 Introduction

Microbubbles are particularly applied in the field of chemical engineering, biomedical engineering, food, aerospace and aviation engineering, etc. For example, they are usually employed as the ultrasound contrast agent [1] because their vibration and breakup enhance the ultrasonic signal and thus provide the required detailed information of the blood flow. Besides, microbubbles have the potential of macromolecular substance mediation which favors their usage for directional therapy of tumors [2] and imaging in the diagnosis of inflammation. In addition, they can be applied in the field of drag reduction [3, 4], mineral flotation [5], wastewater treatment, micro-heat exchangers, fluidized beds [6], etc. With the rapid development of microelectronic mechanical systems (MEMS), microfluidics has been the subject of recent extensive research [7–10]. In comparison to the conventional method of microbubble formation, microbubble production in microfluidic devices has many advantages, such as stable diameter distribution of the disperse phase [11, 12], controllable size of the monodisperse phase [13], high generation frequency [14], etc. Therefore, many researchers have concentrated their interests

on producing microbubbles by microfluidic devices [15–19]. All these applications have special requirements concerning the bubble diameter and its uniformity, so the bubble size is the most critical parameter in microbubble production [20]. To control the size, a profound understanding of the mechanism of bubble generation and breakup is essential.

Microbubbles can be generated using different designs of microfluidic devices, such as a microchannel T-junction, flow focusing device, and other more complicated geometries. Compared with other geometries, that of a T-junction is simple and easy to manufacture. Much effort has been devoted to reveal the mechanism of bubble formation by microchannel T-junctions [21] which is important for successful design of microfluidic devices. At present, numerical simulation is an effective tool to investigate the Taylor bubble formation. Studies of bubble formation in microchannel T-junction mainly focus on bubble generation in Newtonian fluids. Garstecki et al. [13] investigated droplet and bubble formation under low flow rate conditions and proposed an interfacial tension and viscosity-independent empirical relationship between the bubble length and two-phase flow rate ratio: $L/W = 1 + aQ_{in}/Q_{out}$, where L denotes the length of the bubble, W is the width of the channel, Q_{in} and Q_{out} represent the volume flow rate of continuous and disperse phases individually, and a is a channel dimension-dependent parameter. Taha and Cui [22, 23] simulated the motion and deformation of a single Taylor bubble inside capillaries with square and circular cross sections by the volume-of-fluid (VOF) method.

Correspondence: Prof. B. Chen (chenbin@mail.xjtu.edu.cn), Xi'an Jiaotong University, State Key Laboratory of Multiphase Flow in Power Engineering, Xianning West Road No. 28, Xi'an, Shaanxi, 710049, China.

Shao et al. [24] studied the effect of inlet conditions on Taylor flow formation by numerical simulations. The bubble diameter was found to be proportional to the diameter of the gas inflow orifice. In addition, the generated bubble diameter was significantly influenced by surface tension. Qian and Lawal [25] also studied air-water Taylor flow in a T-junction micro-reactor by the VOF method. The influence of flow velocity, surface tension, liquid viscosity, fluid density, and wall-wetting properties on bubble length was investigated and led to the conclusion that the bubble length decreases with the liquid velocity increase but increases with higher gas velocity. Both surface tension and wall-wetting properties affect the bubble length moderately. Guo and Chen [26] carried out a two-dimensional (2D) simulation of Taylor bubble formation in a microchannel T-junction and found a transition capillary number (Ca) from the squeezing regime to the shearing regime of $\sim 5.8 \times 10^{-3}$. Dai et al. [27] simulated the bubble formation in a microchannel T-junction by the VOF model. They focused on the time of bubble detachment and pointed out that the bubble detachment time is mainly controlled by the velocity of the continuous phase but not by the two-phase flow rate ratio. Rong and Chen [28] performed numerical simulation of microbubble generation in a microchannel T-junction by the improved moving particle semi-implicit (MPS) method. Fu et al. [29] experimentally investigated the squeezing-to-dripping transition during the bubble formation in a microfluidic T-junction and applied the two-step model to describe the bubble formation which theoretically predicted the bubble volume well.

For industrial applications, microbubbles in non-Newtonian fluids are frequently encountered. For instance, as an ultrasound contrast agent the microbubbles are added to realize the drug loading and thereby exhibit non-Newtonian behavior. In addition, the bubble behavior in non-Newtonian fluids also plays an important role in the fields of polymer devolatilization, composites processing, boiling, bubble columns, fermentation, plastic foam processing, and bubble absorption [30]. So far, the study of bubble production in non-Newtonian fluids is still very limited. Most of the existing literature about microbubble production in non-Newtonian fluids is about generating bubbles by nozzles submerged in the liquid [31–33]. Considering the aspect of generating monodisperse phases in microfluidic devices, the available investigations which introduced the non-Newtonian properties of the continuous phase are mainly performed in liquid-liquid systems [14, 34, 35].

Recently, Santos and Kawaji [35] compared the computational dimensions of numerical simulations of slug formation in a microchannel T-junction and reported that the surface tension effects cannot be captured correctly by 2D models, especially under the condition of high shearing rates. Similar phenomena were also observed in previous 2D simulations. In this work, 3D simulations were conducted to simulate the bubble generation phenomena in both Newtonian and non-Newtonian fluids. Air was selected as the disperse phase. In order to compare the bubble behavior in Newtonian and non-Newtonian fluid, water, power law fluid, and Bingham fluid were selected as the continuous phase. The viscosity of the

continuous phase was modeled as a power law fluid and as a Bingham fluid to characterize the rheological properties. The influences of the viscosity parameter K , the power law index n , and the yield stress τ_y on the bubble breakup mechanism, shape, size, and generation frequency were investigated.

2 Numerical Method

2.1 Governing Equations

The VOF method was used to track the interface in the numerical simulation. The governing equations for 3D gas-liquid two-phase are:

$$\frac{\partial \rho}{\partial t} + \nabla \cdot (\rho \vec{v}) = 0 \quad (1)$$

$$\frac{\partial (\rho \vec{v})}{\partial t} + \nabla \cdot (\rho \vec{v} \vec{v}) = -\nabla p + \nabla \cdot [\mu (\nabla \vec{v} + \nabla \vec{v}^T)] + \rho \vec{g} + \vec{F}_s \quad (2)$$

In the VOF method, the interfaces between two phases are implicitly captured by the computation of the volume fraction function a_G and a_L , which denote the volume fraction of the gas and liquid phase, respectively. For the cell fully occupied by the gas phase, $a_G = 1$ and $a_L = 0$. For the cell fully occupied by the liquid phase, $a_G = 0$ and $a_L = 1$. For the interface cell, a_G and a_L lie between 0 and 1 and fulfill the relationship: $a_G + a_L = 1$. Therefore, the fluid properties in the interface cells can be calculated by:

$$\rho = a_G \rho_G + (1 - a_G) \rho_L \quad (3)$$

$$\mu = a_G \mu_G + (1 - a_G) \mu_L \quad (4)$$

The volume fraction a_G is convected by the following transport equation:

$$\frac{\partial a_G}{\partial t} + \vec{v} \cdot \nabla a_G = 0 \quad (5)$$

The geometric reconstruction scheme can be implemented to approximate the interface by using a piecewise-linear approach [36]. Pressure Implicit Split-Operator (PISO) is selected as the pressure-velocity coupling algorithm [37], and the Pressure Staggering Option (PRESTO!) scheme is used for the pressure interpolation.

In a microchannel, the inertial force is small and the surface tension force is dominant for a two-phase flow system. The continuum surface force (CSF) model [38] is applied to approximate the surface tension force F_s as a body force in Eq. (2) by the equation:

$$F_s = \sigma \frac{\rho \kappa_G \nabla a_G}{(\rho_G + \rho_L)/2} \quad (6)$$

where σ is the surface tension coefficient. κ_G is the curvature computed from the divergence of the unit surface normal and can be obtained from the following equation:

$$\kappa_G = \nabla \cdot \hat{n} \quad (7)$$

where $\hat{n} = \frac{n}{|n|}$, $n = \nabla a_G$. With the specified contact angle θ , the unit surface normal in the computational cells next to the wall is calculated by:

$$\hat{n} = \hat{n}_w \cos \theta + \hat{t}_w \sin \theta \quad (8)$$

where \hat{n}_w and \hat{t}_w are the unit normal to the wall and unit tangential to the wall, respectively.

2.2 Viscosity Model

The continuous phase is modeled as a Herschel-Bulkley fluid, a type of generalized non-Newtonian fluid model, for which the shear stress τ can be stated as:

$$\begin{cases} \gamma = 0 & \tau \leq \tau_y \\ \tau = \tau_y + K\gamma^n & \tau \geq \tau_y \end{cases} \quad (9)$$

where γ is the strain rate, K is the consistency coefficient, n is the power law exponent, and τ_y is the yield stress.

In the Herschel-Bulkley model, the apparent viscosity will become infinite when $\tau < \tau_y$, which will lead to discontinuity of the calculation. Thus, a high enough initial viscosity μ_0 is defined to describe the apparent viscosity when $\gamma < \tau_y/\mu_0$. The apparent viscosity of the Herschel-Bulkley fluid is given by:

$$\eta = \frac{\tau_y + k[\gamma^n - (\tau_y/\mu_0)^n]}{\gamma} \quad (10)$$

In this study, the initial viscosity μ_0 is set as 1 Pa.s. In the Herschel-Bulkley model, the Newtonian fluid, power law fluid, and Bingham fluid can be represented by taking different values for the rheological parameters K , n , and τ_y in Eq. (10). When $\tau_y = 0$ and $n = 1$, the model describes a Newtonian fluid; when $\tau_y = 0$ and $n \neq 1$, the model defines a power law fluid; when $\tau_y \neq 0$ and $n = 1$, the model expresses a Bingham fluid.

2.3 Model Structure

3D simulations of the micro-bubble generation in a 90° microchannel T-junction were conducted. As illustrated in Fig. 1 a, the dispersed phase is injected into the vertical inlet, while the continuous phase is introduced into the horizontal inlet. The two inlet channels are joined orthogonally to produce bubbles. The whole channel has a rectangular cross section, and four parameters are used to characterize the geometry features for the simulation model: H and W represent the height and width of the straight channel, and H_A and W_A stand for the height and width of the inlet channel for the disperse phase, respectively. The lengths of inlet channels for both continuous phase and disperse phase are $2W$, and the length of the straight channel is $20W$. In order to study the influence of geometrical parameters of the microchannel on the bubble generation, numerical simulations were performed in four microchannel T-junctions with different dimension parameters, as listed in Tab. 1.

In the simulations, air was selected as the disperse phase. In order to compare the bubble behavior in Newtonian and non-

Table 1. Different channel dimension in simulations.

Channel	Channel dimension			
	W [μm]	H [μm]	W_A [μm]	H_A [μm]
I	200	40	200	40
II	200	200	200	200
III	200	200	100	100
IV	200	200	50	50

Newtonian fluid, water, power law fluid, and Bingham fluid were selected as the continuous phase. It is supposed that the whole channel is filled with the continuous phase at the initial time. From $t=0$, the continuous phase and disperse phase were injected into the inlet channels at velocity U_G and U_L . The computational domains were discretized with the GAMBIT mesh generator using hexahedral cells. According to previous experience with VOF, more than 100 cells are necessary to capture the bubble shape precisely on the cross section. Therefore, 20×20 cells are selected for $200 \times 200 \mu\text{m}$ rectangular channel (about 200 cells in the bubble on the channel cross section) and in total 94 000 to 100 000 cells in accordance with the different channel dimensions. Grid-independent results have been obtained for representative simulations as determined by comparison with a verification experiment.

2.4 Validation

In order to validate the numerical algorithm, a visualization experiment was conducted for the air bubble generation in water by a microchannel T-junction. As illustrated in Fig. 1 b, the structure and dimension of the T-junction microchannel in the experiment is the same as channel I in Tab. 1. Distilled water, containing 0.5 wt % sodium dodecyl sulfate (SDS), and air were used as the continuous and disperse phases and were injected into the microchannel T-junction by Harvard PHD2000 and Pump 11 syringe pumps, respectively. A Leica DM-5000 microscope and a Redlake HG-100K high-speed camera were connected to record the process of bubble formation and detaching at a resolution of 1506×456 pixels and 256 bit color. The pictures were captured at the frequency of 1000 fs^{-1} . A microfluidic chip with a T-junction microchannel etched and enclosed in it was used to produce microbubbles. The scheme of the experimental system is presented in Fig. 1 c.

In the simulations, the surface tension coefficient was set at 0.072 N m^{-1} and the wall contact angle of water was set at 0° . Fig. 2 displays four snapshot flow patterns of bubble generation at the crossing domain of channel I by the visualization experiment and numerical simulation, respectively. The bubble shape is quite similar in the experiment and simulation which confirms that the algorithm can track the interface of a Taylor bubble very well. Fig. 2 c compares the bubble lengths between experiment and numerical simulation for different U_G and U_L . The calculated bubble lengths fall into the same region with those of the experiment which also validates the algorithm.

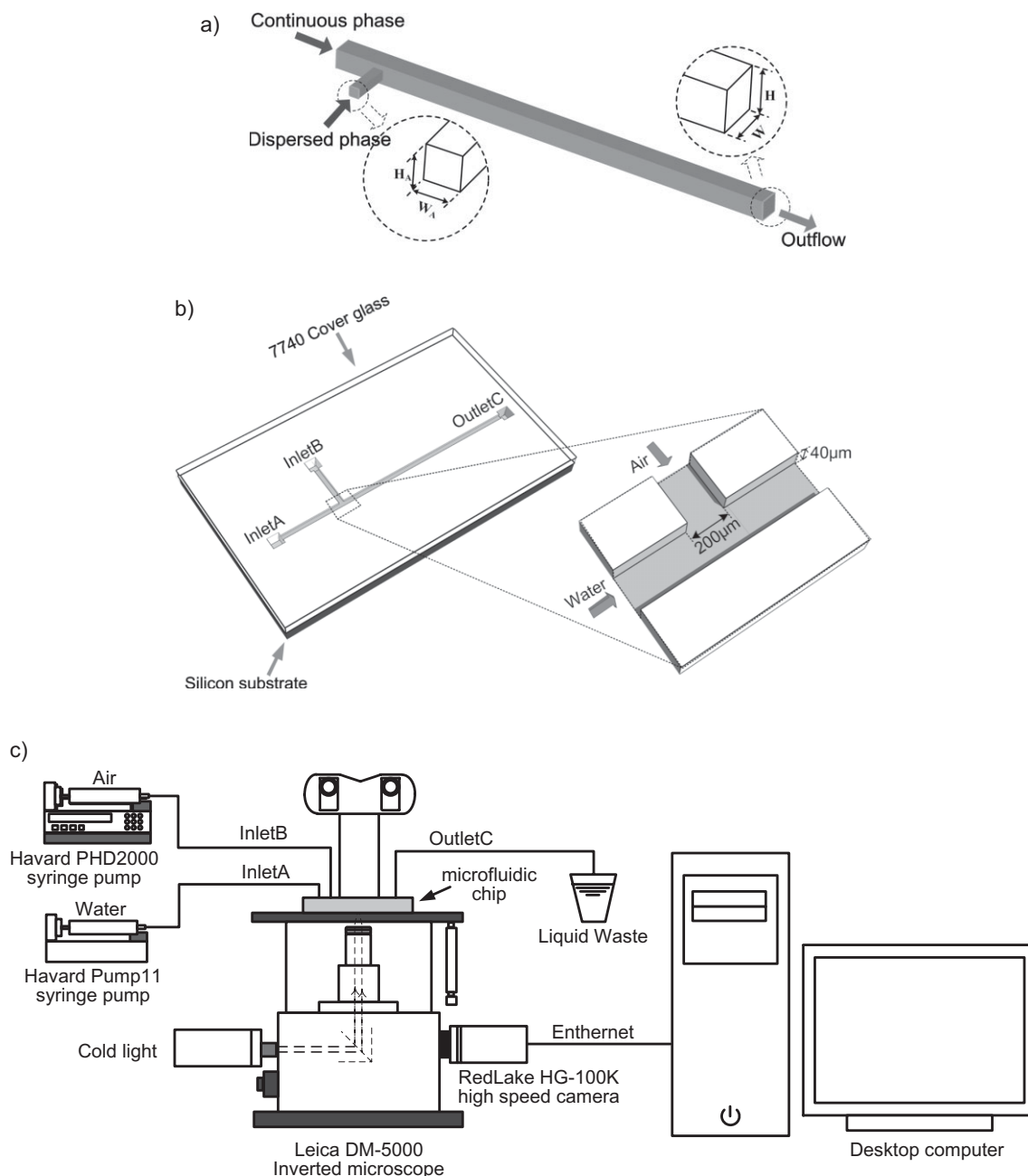


Figure 1. Flow visualization experimental system. a) Schematic diagram of the microchannel T-junction in the simulation. b) Geometry of the microfluidic chip with channel I. c) Scheme of the experimental system.

3 Results and Discussion

3.1 Bubble Generation in Newtonian Fluids

3.1.1 Bubble Breakup Mechanism

So far, a lot of experiments and numerical simulations have declared that there exist two different mechanisms: a squeezing regime and a shearing regime, which is commonly called dripping regime in liquid-liquid flow, for bubble or droplet breakup

in the microchannel T-junction under different inlet velocity, interfacial force, or viscosity conditions. Both breakup mechanisms apparently influence the shape, size, and generation frequency of the bubbles. Usually, Ca is an important dimensionless number to characterize the bubble breakup mechanism:

$$Ca = \frac{\mu_c U_c}{\sigma} \quad (11)$$

where μ_c and U_c are the characteristic viscosity and velocity, respectively. Ca represents the relative effect of viscous forces

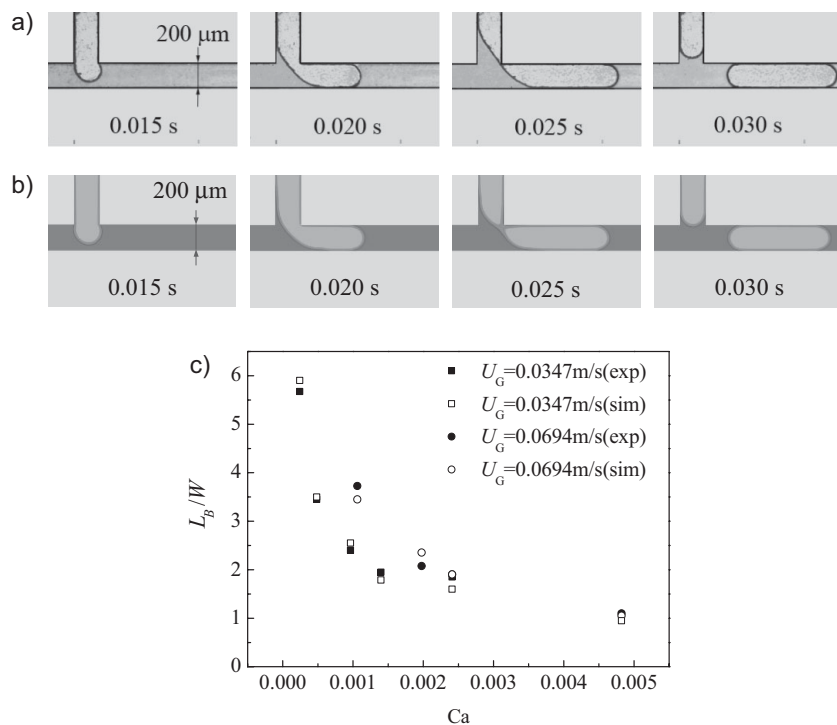


Figure 2. Comparison between visualization experiment and numerical simulation of bubble formation (channel I). a) Visualization experiment ($U_G = U_L = 0.0347 \text{ m s}^{-1}$, $Re_{\text{cont}} = 6.93$, $Ca = 4.82 \times 10^{-4}$); b) numerical simulation; same conditions as for (a); c) comparison of bubble length for different U_G and U_L .

versus surface tension acting across an interface in a microfluidic system. In this work, the viscosity and velocity of the continuous phase were selected as μ_c and U_c for the discussion and both of the breakup mechanisms were obtained.

At low Ca , the Taylor flow is dominated by the interfacial force, and the disperse phase (air) will penetrate into the continuous phase (water). As demonstrated in Fig. 3 a, the gas-liquid interface will expand and block the entire liquid flow. Then the continuous phase pushes the disperse phase forward until the interface breaks at the downstream corner of the junction. This breakup mechanism is the squeezing regime.

By contrast, the Taylor flow is dominated by the viscous force while Ca is relatively high. The disperse phase will be sheared off by the continuous phase before it fully penetrates into the straight channel. As indicated in Fig. 4 a, a long and thin neck of the gas-liquid interface will form and finally split at the location after the downstream corner of the junction. This breakup mechanism is the shearing regime.

Figs. 3 b–e display the stream-wise velocity distribution of the continuous phase for different cross sections of the horizontal channel in the squeezing regime. In Fig. 3 a, A–A' ($x = 554 \mu\text{m}$), B–B' ($x = 600 \mu\text{m}$), C–C' ($x = 640 \mu\text{m}$), and D–D' ($x = 1012 \mu\text{m}$) cross sections denote the positions near the junction corner and bubble head, respectively. It can be concluded from Figs. 3 b–e that the gas velocity is higher than the ambient liquid at the neck of the undetached bubble and the highest velocity exists in the narrowest position of the neck which is caused by the push of the liquid phase and the narrow cross section of the flow. On the B–B' cross section, the ratio between the gas maximal velocity and the average velocity in the horizontal channel is $U_{\text{max}}/U_{\text{ave}} > 4$, while in the head of the bubble, there also exists a high liquid velocity region in the

gap between bubble and the channel wall. Fig. 3 f illustrates the vorticity distribution on the D–D' cross section in the squeezing regime. The vorticities are found to be quite small at the corner of the channel, and the larger vorticities are mainly located in the interface of the bubbles where the velocity gradients are bigger than those at the corner because of the different phase properties under the same surface tension in both sides of the interface.

Figs. 4 b–e present the stream-wise velocity distribution of the continuous phase for different cross sections of the horizontal channel in the shearing regime. In comparison with the squeezing regime, the influence of the shearing regime on the velocity of the continuous phase is quite smaller, the neck is smaller. In the neck region, the ratio between the gas maximal velocity and average velocity in the horizontal channel is $U_{\text{max}}/U_{\text{ave}} > 5.7$. Fig. 4 f also shows the vorticity distribution on the D–D' cross section in the shearing regime. As in the squeezing regime, vorticities are also located in the interface of the bubbles.

3.1.2 Effect of Velocities of Two Phases on Bubble Formation

Channel II is employed to study the effect of the velocity ratio between the two phases on bubble formation. Different simulation cases are summarized in Tab. 2. Fig. 5 indicates the bubble length and frequency change with Q_L/Q_G as well as the corresponding flow patterns for different gas velocities U_G . Generally, the bubble breakup mechanism is the squeezing regime when the velocity of the continuous phase is relatively low. In the case of increasing velocity of the continuous phase, the breakup mechanism transits gradually to the shearing re-

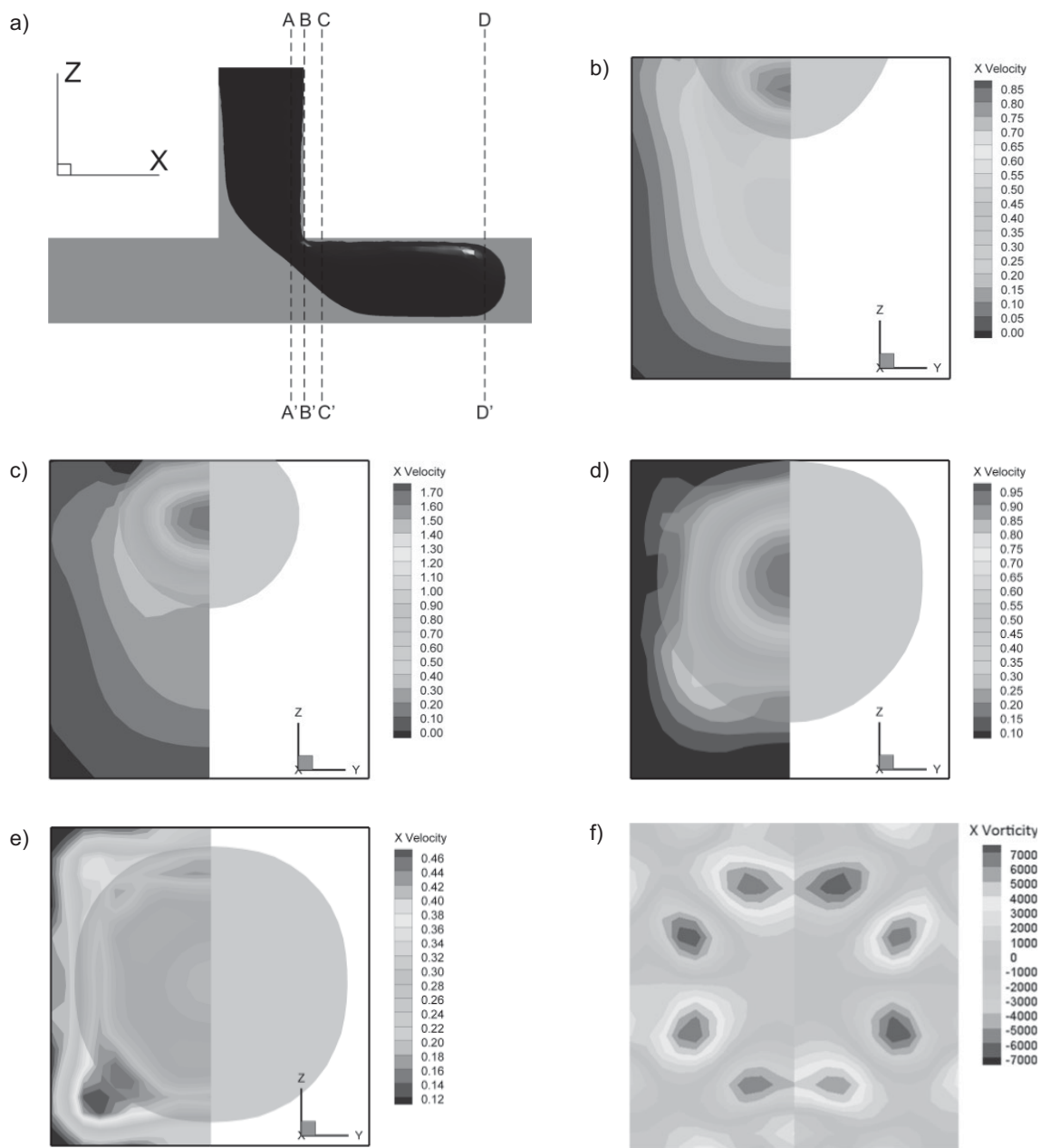


Figure 3. Flow pattern of squeezing regime and cross-sectional view of stream-wise velocity distribution of the continuous phase in the horizontal channel ($U_G = 0.1 \text{ m s}^{-1}$, $U_L = 0.3 \text{ m s}^{-1}$, $Re_{\text{cont}} = 59.89$, $Ca = 4.12 \times 10^{-3}$, $t/T = 0.9$). a) Flow pattern of the squeezing regime; b) A–A' cross section; c) B–B' cross section; d) C–C' cross section; e) D–D' cross section; f) vorticity distribution on D–D' cross section.

Table 2. Different simulation cases to study the effect of superficial velocity on bubble formation.

Q_L/Q_G	$U_G [\text{m s}^{-1}]$	$U_L [\text{m s}^{-1}]$	Ca	Re_{cont}	Re_{dis}
1:1–6:1	0.02	0.02–0.12	2.79×10^{-4} – 1.67×10^{-4}	3.99–23.96	0.27
1:1–6:1	0.1	0.10–0.60	1.39×10^{-3} – 8.36×10^{-3}	19.96–199.64	1.37
1:1–6:1	0.2	0.20–1.20	2.79×10^{-3} – 1.67×10^{-2}	39.93–239.57	2.74

gime and the bubble length decreases correspondingly. The frequency of bubble formation rises with higher velocity ratio between the two phases, and the frequency increases faster while the gas velocity is higher.

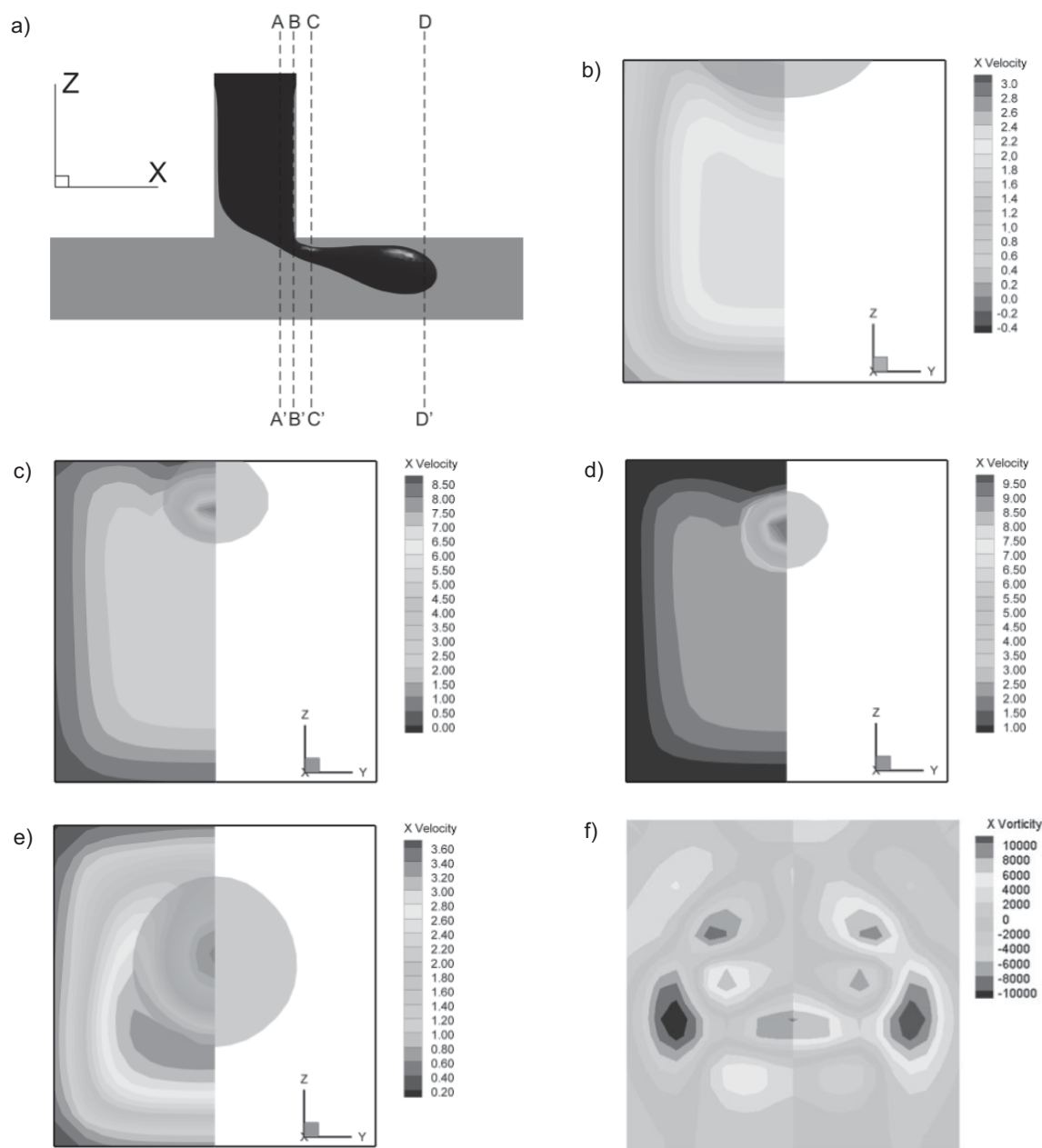


Figure 4. Flow pattern of the shearing regime and cross-sectional view of stream-wise velocity distribution of the continuous phase in the horizontal channel ($U_G = 0.2 \text{ m s}^{-1}$, $U_L = 1.6 \text{ m s}^{-1}$, $Re_{\text{cont}} = 319.92$, $Ca = 2.2 \times 10^{-2}$, $t/T = 0.9$). a) Flow pattern of the shearing regime; b) A–A' cross section; c) B–B' cross section; d) C–C' cross section; e) D–D' cross section; f) vorticity distribution on D–D' cross section.

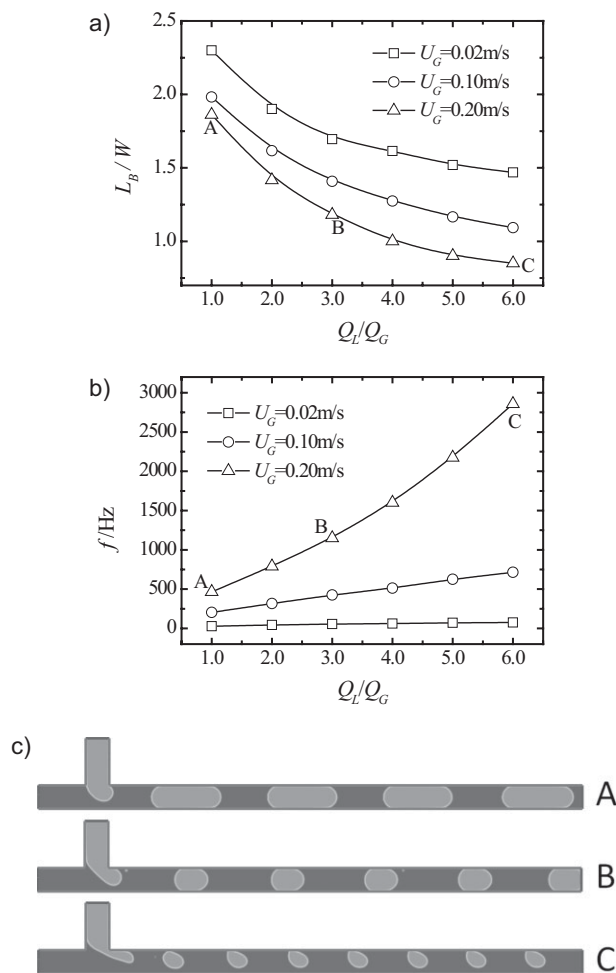
3.1.3 Effect of Cross-Sectional Area of the Disperse Phase Inlet on Bubble Formation

Channel II, III, and IV were used to study the influence of the cross-sectional area of the disperse phase inlet on bubble formation. Different simulation cases are listed in Tab. 3. For these three channels, the cross-sectional area S_{dis} is different and $S_{\text{II}} = 4S_{\text{III}} = 16S_{\text{IV}}$. In order to ensure the same volume flow rate of the dispersed phase, the inlet velocity satisfies $16U_{\text{GII}} = 4U_{\text{GIII}} = U_{\text{GIV}}$.

According to the statistics from the simulation results, the transition capillary numbers for the three channels are 5.6×10^{-3} , 8.36×10^{-3} , and 1.2×10^{-2} . Therefore, it can be concluded that the smaller the cross-sectional area of the disperse phase inlet is, the more likely the bubbles will be generated by the shearing regime mechanism and the smaller the size of the bubbles obtained in horizontal channel will be. Higher generation frequency will be beneficial to the generation of micro-bubbles.

Table 3. Different simulation cases to study the effect of the cross-sectional area of the disperse phase inlet on bubble formation.

Channel	Velocity		Ca	Re _{cont}	Re _{dis}
	U_G [m s ⁻¹]	U_L [m s ⁻¹]			
II	0.1	0.1–1.0			
III	0.4	0.1–1.0	1.39×10^{-3} – 1.39×10^{-2}	19.96–199.64	1.37
IV	1.6	0.1–1.0			

**Figure 5.** Effect of velocity ratio between the two phases on bubble formation. a) Bubble length change with different Q_L/Q_G ; b) bubble frequency change with different Q_L/Q_G ; c) transition from squeezing regime to shearing regime.

3.2 Bubble Generation in a Power Law Fluid

The VOF model is used to study bubble formation in non-Newtonian fluids by a microchannel T-junction. The viscosity of the continuous phase was modeled as a power law fluid and a Bingham fluid, respectively. The influences of the viscosity parameter K , the power law index n , and the yield stress τ_y

on the bubble breakup mechanism, shape, size, and generation frequency were investigated sequentially. In non-Newtonian fluid, Ca can be calculated using the apparent viscosity which can be acquired with Eq. (10).

3.2.1 Effect of Viscosity Parameter K and Power Law Index n

In the power law fluid model, the apparent viscosity is defined by the viscosity coefficient K and the power law index n . Here, bubble generation is investigated in a power law fluid by changing both parameters in channel III. The inlet velocities of the continuous phase and dispersed phase were $U_G = 0.1$ m s⁻¹ and $U_L = 0.4$ m s⁻¹, respectively. Values of K and n are listed in Tab. 4 together with the simulation parameters.

Fig. 6 illustrates the effect of n and K on bubble generation, where A, B, and C denote $K = 0.023$ and $n = 0.66, 0.81, 0.9$, respectively. The bubble diameter decreases and the generation frequency increases with higher K and n . An obvious transition of the bubble breakup mechanism from the squeezing regime to the shearing regime is observed, and the bubble shape becomes irregular during this process. The bubble size decreases approximately linearly with the increase of the power law index n . The bubble generation frequency increases when the bubble breakup mechanism changes from the squeezing regime to the shearing regime.

The effect of K on bubble generation is easy to explain. Hong and Li [39] found that the velocity distribution is independent of K for a power law fluid in circular pipes. Sang et al. [14] pointed out that this conclusion can also be extended to channels with non-circular cross sections. According to Eq. (10), K is directly proportional to the apparent viscosity of the continuous phase. Therefore, the apparent viscosity of the continuous phase increases with higher K , and the bubble diameter reduces with higher viscous force.

The influence of n on bubble generation can be explained by its effect on the apparent viscosity of the continuous phase and its velocity distribution in the straight channel. The apparent viscosity of the continuous phase obviously becomes higher with the increase of n , while the velocity distributions remain unchanged. Consequently, the bubble diameter will decrease with higher n .

Table 4. Simulation parameters for investigating the effect of K and n in the power law fluid.

K [Pa s ^{n}]	n	Ca	Re _{cont}	Re _{dis}
0.001		0.015–0.20		
0.023	0.66, 0.71, 0.78, 0.81, 0.86, 0.9, 1.0	0.035–0.46	7.99–330.99	1.37
0.035		0.053–0.70		

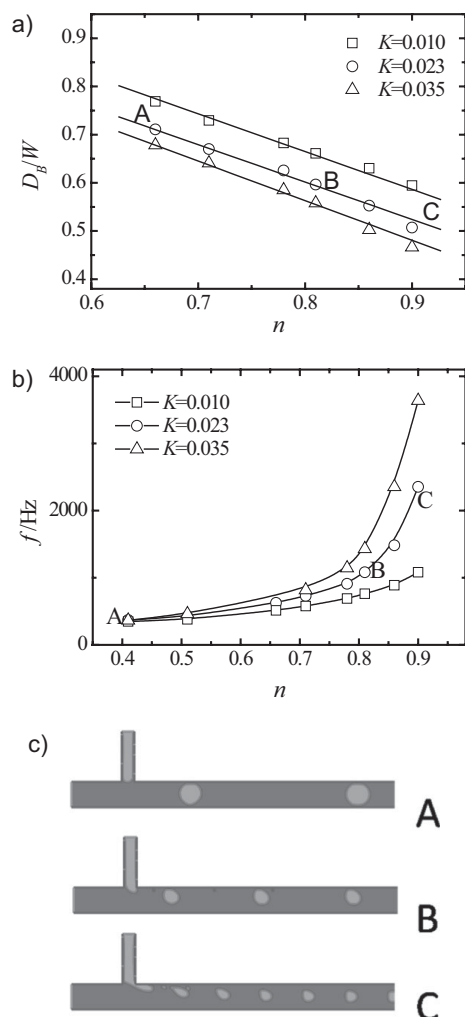


Figure 6. Effect of power law index n on bubble generation ($U_G = 0.1 \text{ m s}^{-1}$, $U_L = 0.4 \text{ m s}^{-1}$). a) Effect of n on bubble size; b) effect of n on bubble generation frequency; c) flow pattern in the channel at different n .

3.2.2 Comparison of Bubble Generation in Power Law and Newtonian Fluids

For power law fluids, microbubbles are also generated by the same two mechanisms, i.e., the squeezing regime and shearing regime. In addition, the bubble shape is also very similar to that of bubbles generated in a Newtonian fluid. The difference is the influence of fluid viscosity on the bubble size for the same Ca . Therefore, the bubble diameter D_B as a function of Ca for the bubble generation in power law and Newtonian fluids was compared by changing U_L and U_G at constant flow rate ratio $Q_L/Q_G = 4$. Detailed simulation parameters are listed in Tab. 5.

Table 5. Simulation parameters for investigating the difference of bubble generation in power law and Newtonian fluids.

Channel	Q_L/Q_G	$U_G [\text{m s}^{-1}]$	$U_L [\text{m s}^{-1}]$	Ca	Re_{cont}	Re_{dis}
III	4:1	0.02–0.4	0.08–1.6	1.13×10^{-3} – 2.23×10^{-2}	39.93–319.92	0.06–5.47

Table 6. Simulation parameters for investigating the effect of channel dimension.

Channel	$U_L [\text{m s}^{-1}]$	$U_G [\text{m s}^{-1}]$	$K [\text{Pa s}^n]$	n	Ca	Re_{cont}	Re_{dis}
II		0.025			0.015–0.20		
III	0.4	0.10	0.023	0.66, 0.71, 0.78, 0.81, 0.86, 0.9	0.035–0.46	7.99–330.99	1.37
IV		0.40			0.053–0.70		

The Ca – D_B relation in the Newtonian fluid is compared in Fig. 7 with that obtained in the power law fluid by changing the power law index n . The rate of reduction of bubble diameter in the power law fluid is slower than that in the Newtonian fluid as a function of Ca . In the power law fluid, the bubble diameter decreases by 34.5 %, from $1.16W$ to $0.76W$ as the Ca changes from 0.01 to 0.21. In the Newtonian fluid, the bubble diameter is reduced by 45.6 %, from $1.36W$ to $0.74W$ as the Ca alters from 0.001 to 0.023. This result indicates that the effect of viscous force on bubble generation is more obvious in Newtonian fluids than in power law fluids. The transition from the squeezing regime to the shearing regime occurred at $Ca = 0.05$ for the power law fluid and for the Newtonian fluid at $Ca = 8.36 \times 10^{-3}$.

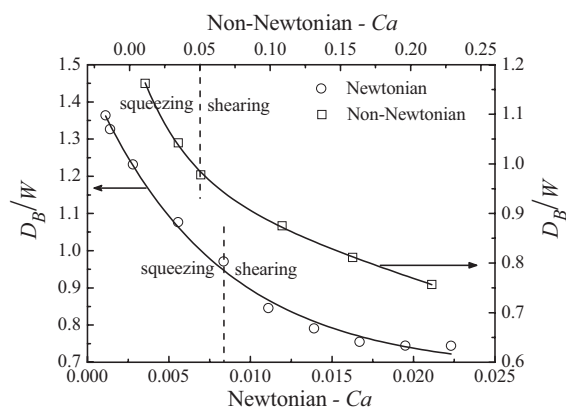


Figure 7. Comparison of bubble generation between power law and Newtonian fluids ($U_G = 0.1 \text{ m s}^{-1}$, $U_L = 0.4 \text{ m s}^{-1}$).

3.2.3 Effect of Channel Dimension

The effect of channel dimension on bubble generation is investigated in channel II, III, and IV at the same gas-liquid volume flow rate ratio Q_L/Q_G . Detailed simulation parameters are summarized in Tab. 6.

Fig. 8 presents the effect of n on bubble generation for the power law fluid in channel II, III, and IV. The bubble diameter

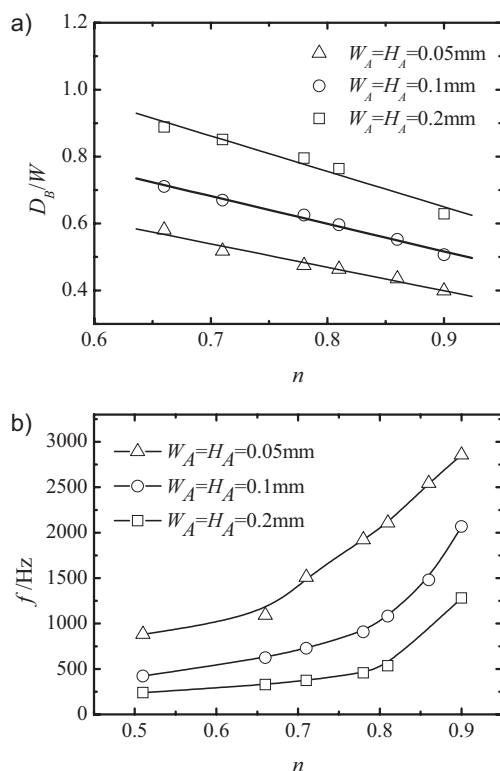


Figure 8. Effect of power law index n on bubble generation for three different channel dimensions ($U_G=0.1\text{ m s}^{-1}$, $U_L=0.4\text{ m s}^{-1}$). a) Effect of n on bubble diameter; b) effect of n on bubble generation frequency.

decreases and the generation frequency increases with higher n . With the reduction of the cross-sectional area of the dispersed phase inlet, the bubble diameter becomes smaller and the generation frequency rises. In channel III, bubbles with diameters smaller than $0.4W$ can be produced. This implies that reducing the cross-sectional area of the dispersed phase inlet is effective for control of the bubble diameter when the bubble size is required to be smaller than the channel dimension.

3.3 Bubble Generation in a Bingham Fluid

In the Bingham fluid model, the apparent viscosity is defined by the viscosity coefficient K and the yield stress τ_y . Here, the effect of these two parameters on the bubble generation is investigated. The average inlet velocities of the continuous phase

and the dispersed phase were $U_G=0.1\text{ m s}^{-1}$ and $U_L=0.4\text{ m s}^{-1}$. Detailed parameters of K and τ_y are presented in Tab. 7.

3.3.1 Effect of Viscosity Coefficient K

Figs. 9 a and b illustrate the influence of K on the bubble size and generation frequency in channel II and III. As K increases from 0.002 to 0.04 Pa s^n at $\tau_y=200\text{ Pa}$ in channel II, the bubble diameter changes from $0.54W$ to $0.61W$, and the variation range is 11.67 %. The variation of the bubble size with higher K is negligibly small, and the variation of the bubble generation frequency is also very small as demonstrated in Fig. 9 b. The same conclusion on the effect of K in channel III with $\tau_y=500\text{ Pa}$ is also indicated in Figs. 9 a and b.

The impact of K on the bubble formation in the Bingham fluid can be explained by the span-wise distributions of apparent viscosity and velocity in the straight channel which are displayed in Figs. 9 c and d in accordance with channel II. The apparent viscosity is reduced, while the velocity increased significantly with higher K in the region of $y=100\text{--}200\text{ }\mu\text{m}$, where bubbles may be generated. The influence of apparent viscosity and velocity balanced each other, and therefore the bubble size and generation frequency will not change greatly with different K .

3.3.2 Effect of Yield Stress τ_y

In order to evaluate the effect of the yield stress τ_y , its value was varied from 100 to 300 Pa at $K=0.002\text{ Pa s}$. Fig. 10 illustrates the change of bubble shape and viscosity distribution for $\tau_y=100, 200$, and 300 Pa.

Fig. 11 indicates the 3D bubble shape, viscosity, and velocity distribution at the bubble's center cross section at $\tau_y=100, 200$, and 300 Pa, where the shadow region represents the gas phase.

For the Bingham fluid, the bubble generation mechanism and the bubble size remained unchanged for varying Ca . The influence of the rheological property on bubble generation can be represented by the effect of yield stress on the bubble shape. From Figs. 10 a and 11 a–c it follows that the bubble shape changes from spherical to flat ellipsoidal. This phenomenon may be explained by the high-viscosity plug region due to the yield stress. The shear rate is lowest in the central area of the channel cross section, consequently there a high-viscosity region will be formed which will become wider with higher τ_y , as shown in Figs. 10 b and 11 d–f. The bubble becomes flatter under the squeeze of this region.

Table 7. Physical properties of the working fluids for investigating the effect of K in the Bingham fluid.

Channel	U_L [m s^{-1}]	U_G [m s^{-1}]	K [Pa s^n]	τ_y [Pa]	Ca	Re_{cont}	Re_{dis}
II	0.4	0.1	0.002–0.04	100, 200, 300, 500	0.015–0.20	7.99–330.99	1.37
III				100, 200, 300, 500	0.053–0.70		

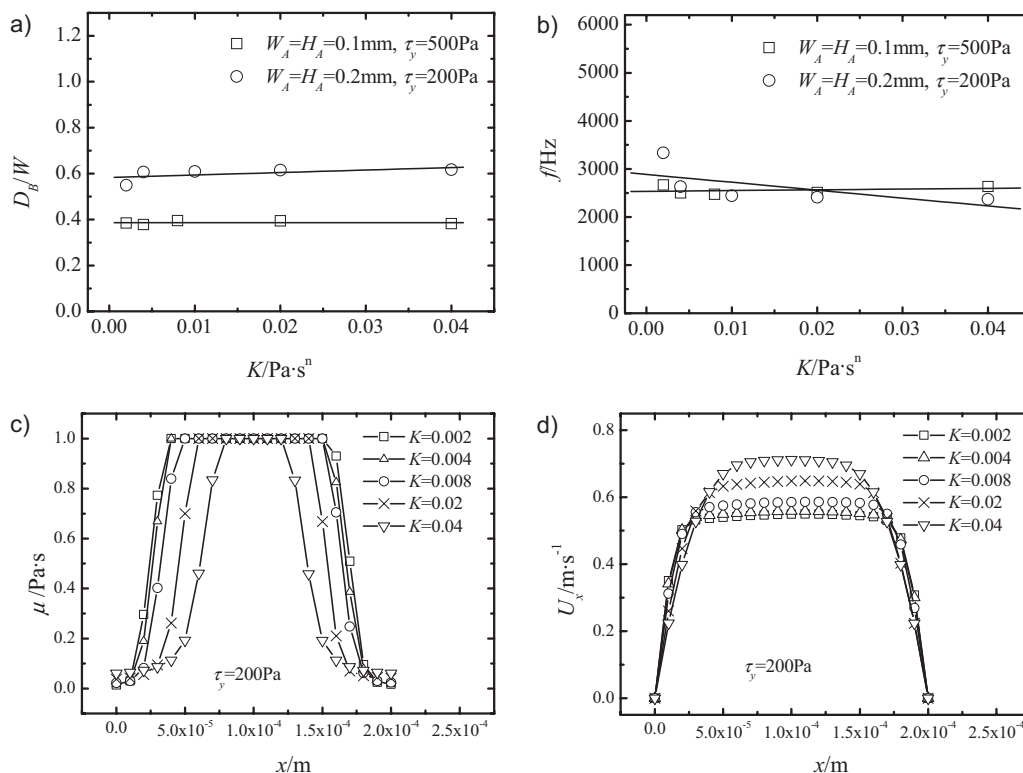


Figure 9. Effect of K on bubble generation in the Bingham fluid ($U_G = 0.1 \text{ m s}^{-1}$, $U_L = 0.4 \text{ m s}^{-1}$). a) Effect of K on the bubble diameter; b) effect of K on the bubble frequency; c) span-wise viscosity distribution (channel II); d) span-wise velocity distribution (channel II).

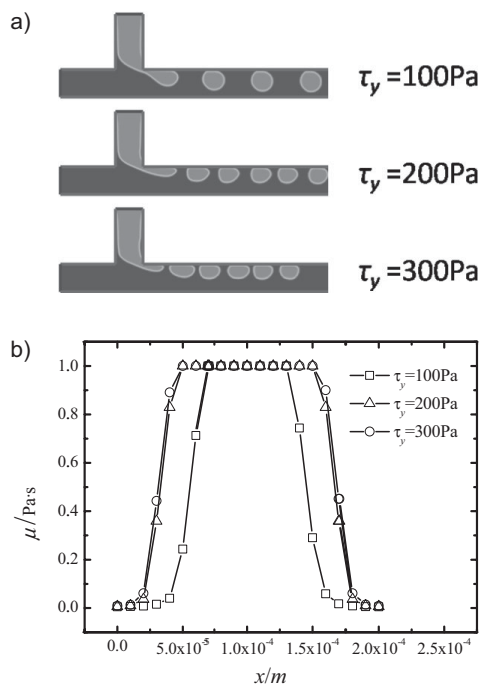


Figure 10. Effect of yield stress τ_y of the Bingham fluid on bubble formation ($U_G = 0.1 \text{ m s}^{-1}$, $U_L = 0.4 \text{ m s}^{-1}$). a) Bubble shape at different values of τ_y ; b) span-wise viscosity distribution at different values of τ_y .

3.3.3 Relationship Between Bubble Diameter and Frequency

Cramer et al. [40] proposed an empirical correlation for the bubble diameter and frequency generated in a Newtonian fluid in a microchannel:

$$D_B = \sqrt[3]{\frac{6}{\pi} Q_{\text{dis}} T_n} \quad (12)$$

where Q_{dis} is the flow rate of the disperse phase and T_n is the drip interval between successive drops. Fig. 12 illustrates the relationship between the bubble diameter and frequency in the non-Newtonian fluid compared with Cramer's correlation. The simulation results are in good agreement with the correlation which implies that Cramer's correlation can be extended to power law fluid and Bingham fluids.

4 Conclusions

3D simulations of bubble generation in both Newtonian and non-Newtonian fluids were conducted in a microchannel T-junction by the VOF model. The numerical results are in good agreement with experimental measurements which provided the validation of the numerical model. A comprehensive description of the bubble breakup mechanism is achieved. Numerical results demonstrate that microbubbles will break

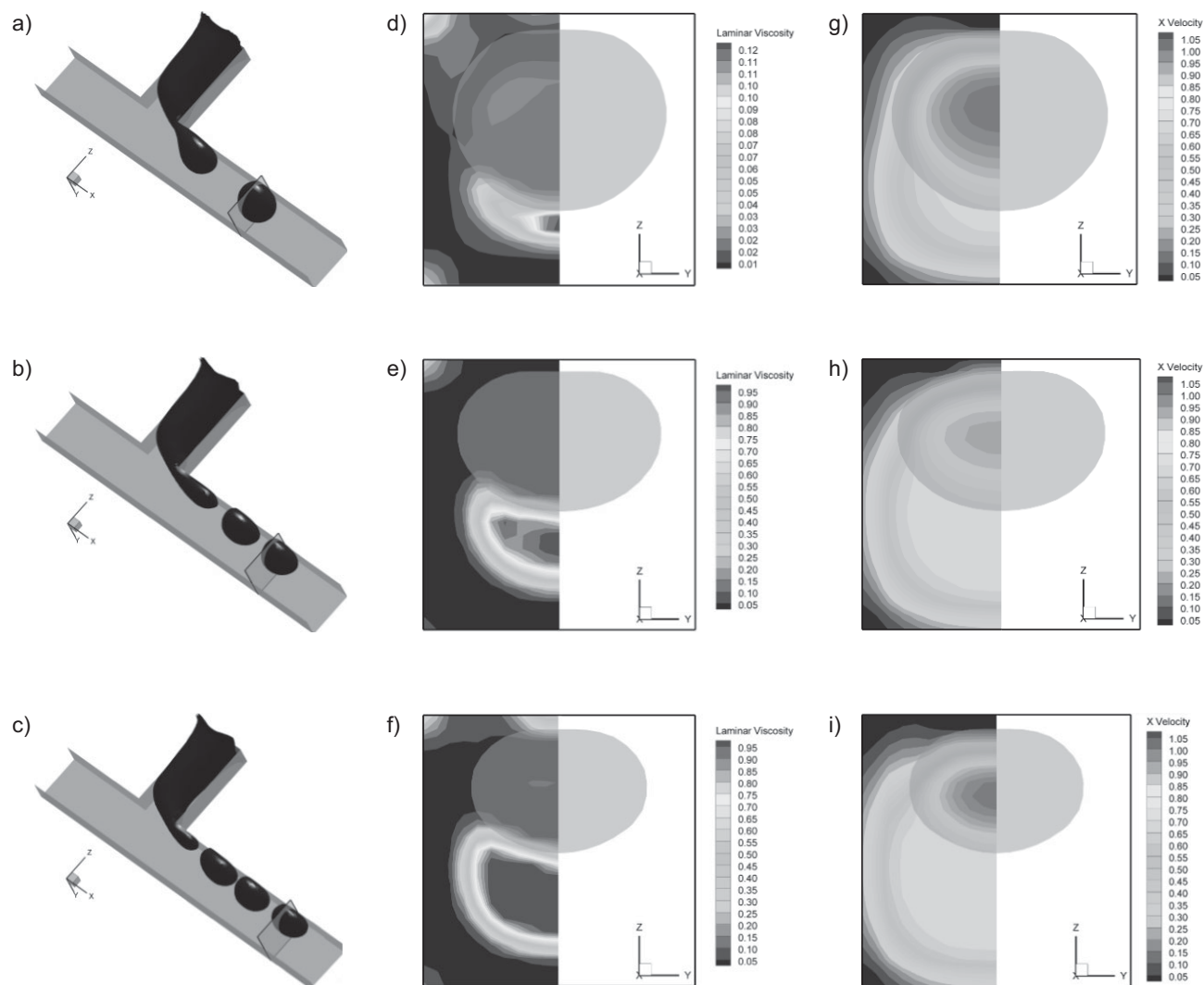


Figure 11. Viscosity and velocity distributions at different vertical cross sections in the Bingham fluid ($U_G = 0.1 \text{ m s}^{-1}$, $U_L = 0.4 \text{ m s}^{-1}$). a) $\tau_y = 100 \text{ Pa}$; b) $\tau_y = 200 \text{ Pa}$; c) $\tau_y = 300 \text{ Pa}$; d) viscosity distribution ($x = 1.012 \text{ mm}$); e) viscosity distribution ($x = 1.112 \text{ mm}$); f) viscosity distribution ($x = 1.214 \text{ mm}$); g) velocity distribution ($x = 1.012 \text{ mm}$); h) velocity distribution ($x = 1.112 \text{ mm}$); i) velocity distribution ($x = 1.214 \text{ mm}$).

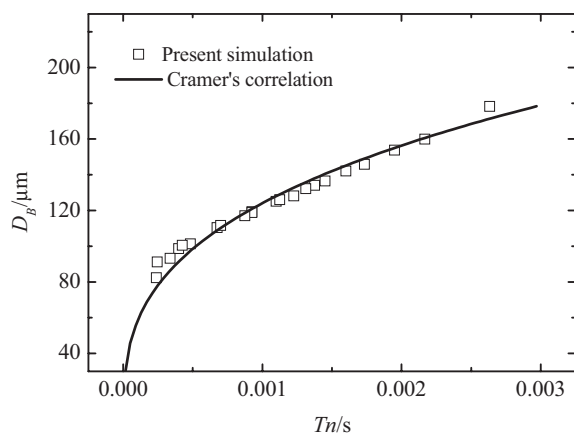


Figure 12. Relationship between bubble diameter and frequency.

off in a squeezing regime for the low Ca condition and in a shearing regime for the high Ca condition.

For the bubble generation in Newtonian fluid, the critical Ca which dominates the transition of the bubble breakup mechanism is dependent on the velocity ratio of two phases and on the microchannel dimension. The bubble diameter is mainly determined by the velocity ratio between the two phases and almost independent of the velocity of the two phases under high-velocity conditions. For the three channels, disperse phase inlet channels of $200 \times 200 \mu\text{m}^2$, $100 \times 100 \mu\text{m}^2$, $50 \times 50 \mu\text{m}^2$, transition capillary numbers of 5.6×10^{-3} , 8.36×10^{-3} , and 1.2×10^{-2} were determined. The smaller the cross-sectional area of the disperse phase inlet, the more likely the bubbles will be generated by the shearing regime mechanism to get the smaller bubbles.

For the non-Newtonian fluid, the viscosity of the continuous phase was modeled as a power law fluid and as a Bingham fluid. The influences of the viscosity parameter K , the power law index n , and the yield stress τ_y on the bubble breakup mechanism, shape, size, and generation frequency were investigated. The main conclusions are as follows:

(i) For the power law fluid, the bubble diameter decreases and the generation frequency increases with higher K and n . The bubble size is reduced approximately linearly with the increase of the power law index n . The bubble generation frequency becomes higher when the bubble breakup mechanism changes from the squeezing regime to the shearing regime.

(ii) Comparing with Newtonian fluid, the influence of the viscous force on bubble generation in the power law fluid is smaller, the bubble diameter decreases slower with the increase of Ca , and the critical Ca which denotes the bubble breakup mechanism transiting from the squeezing regime to the shearing regime is higher. The transition from the squeezing regime to the shearing regime occurred at $Ca = 0.05$ for the power law fluid and at $Ca = 8.36 \times 10^{-3}$ for the Newtonian fluid for the $100 \times 100 \mu\text{m}^2$ disperse phase inlet and $200 \times 200 \mu\text{m}^2$ main channel.

(iii) In Bingham fluids, a high-viscous region is developed in the central area of the channel due to the yield stress τ_y . Bubbles deform to a flat ellipsoid shape under the squeezing of this highly viscous region. Bubble diameter and generation frequency are almost independent of K .

(iv) An empirical correlation for the bubble diameter and frequency proposed by Cramer can be extended to power law and Bingham fluids.

Acknowledgment

This research was financially supported by the National Science Foundation of China (No. 51176152, No. 51336006) and the Specialized Research Fund for the Doctoral Program of Higher Education (No. 20120201110070) and the Fundamental Research Funds for the Central Universities.

The authors have declared no conflict of interest.

Symbols used

Ca	[–]	capillary number
D_B	[μm]	bubble diameter
f	[Hz]	frequency of bubble formation
F_s	[N]	surface tension force
H	[μm]	depth of the straight channel
H_A	[μm]	depth of the inlet channel for the disperse phase
K	[Pa s^n]	consistency coefficient
L_B	[μm]	bubble length
n	[–]	power law index
\hat{n}_w	[–]	unit normal to the wall
Q_{dis}	[$\text{m}^3 \text{s}^{-1}$]	flow rate of the disperse phase
Q_G	[mL h^{-1}]	volumetric flow rate of gas
Q_L	[mL h^{-1}]	volumetric flow rate of liquid

Re_{cont}	[–]	Reynolds number of the continuous phase
Re_{dis}	[–]	Reynolds number of the disperse phase
S_{dis}	[m^2]	cross-sectional area of the disperse phase unit tangential to the wall
\hat{t}_w	[–]	drip interval between successive drops
T_n	[s]	average velocity in the horizontal channel
U_{ave}	[m s^{-1}]	velocity of the continuous phase
U_c	[m s^{-1}]	velocity of the gas phase
U_G	[m s^{-1}]	velocity of the liquid phase
U_L	[m s^{-1}]	gas maximal velocity in the horizontal channel
U_{max}	[m s^{-1}]	width of the straight channel
W	[μm]	width of the inlet channel for the disperse phase
W_A	[μm]	

Greek symbols

α_G	[–]	volume fraction function of gas
α_L	[–]	volume fraction function of liquid
γ	[s^{-1}]	strain rate
η	[Pa s]	apparent viscosity
κ_G	[m^{-1}]	surface curvature
μ_0	[Pa s]	initial viscosity
μ_c	[Pa s]	viscosity of the continuous phase
θ	[°]	contact angle
ρ_g	[kg m^{-3}]	density of the gas phase
ρ_l	[kg m^{-3}]	density of the liquid phase
σ	[N m^{-1}]	surface tension coefficient
τ_y	[Pa]	yield stress

References

- [1] S. Mazziotti, F. Zimbaro, A. Pandolfo, S. Racchiusa, N. Settineri, G. Ascenti, *Abdom. Imaging* **2010**, 35 (2), 241–245.
- [2] T. Nishioka, H. Luo, M. C. Fishbein, B. Cercek, J. S. Forrester, C. J. Kim, H. Berglund, R. J. Siegel, *J. Am. Coll. Cardiol.* **1997**, 30 (2), 561–568.
- [3] Q. L. Lu, H. D. Liang, T. Partridge, M. Blomley, *Gene Ther.* **2003**, 10 (5), 396–405.
- [4] N. K. Madavan, S. Deutsch, C. L. Merkle, *AIAA Pap.* **1984**, 84-0348.
- [5] T. Takahashi, T. Miyahara, H. Mochizuki, *J. Chem. Eng. Jpn.* **1979**, 12 (4), 275–280.
- [6] S. Movahedirad, M. Ghafari, A. M. Dehkordi, *Chem. Eng. Technol.* **2012**, 35 (5), 929–936.
- [7] G. Griffini, A. Gavrilidis, *Chem. Eng. Technol.* **2007**, 30 (3), 395–406.
- [8] D. M. Fries, F. Trachsel, P. R. von Rohr, *Int. J. Multiphase Flow* **2008**, 34 (12), 1108–1118.
- [9] D. M. Fries, P. R. von Rohr, *Chem. Eng. Sci.* **2009**, 64 (6), 1326–1335.
- [10] N. Shao, A. Gavrilidis, P. Angeli, *Chem. Eng. J.* **2010**, 160 (3), 873–881.
- [11] P. Garstecki, I. Gitlin, W. Diluzio, G. M. Whitesides, E. Kumacheva, H. A. Stone, *Appl. Phys. Lett.* **2004**, 85 (13), 2649–2651.

- [12] T. T. Fu, Y. G. Ma, D. Funfschilling, H. Z. Li, *Chem. Eng. Sci.* **2009**, *64* (10), 2392–2400.
- [13] P. Garstecki, M. J. Fuerstman, H. A. Stone, G. M. Whitesides, *Lab Chip* **2006**, *6* (3), 437–446.
- [14] L. Sang, Y. P. Hong, F. J. Wang, *Microfluid. Nanofluid.* **2009**, *6* (5), 621–635.
- [15] A. M. Ganan-Calvo, *Phys. Rev. E: Stat., Nonlinear, Soft Matter Phys.* **2004**, *69*, 027301.
- [16] T. Cubaud, C. M. Ho, *Phys. Fluids* **2004**, *16* (12), 4575–4585.
- [17] J. M. Gordillo, Z. D. Cheng, A. M. Ganan-Calvo, M. Marquez, D. A. Weitz, *Phys. Fluids* **2004**, *16* (8), 2828–2834.
- [18] K. Hettiarachchi, E. Talu, M. L. Longo, P. A. Dayton, A. P. Lee, *Lab Chip* **2007**, *7* (4), 463–468.
- [19] V. van Steijn, M. T. Kreutzer, C. R. Kleijn, *Chem. Eng. Sci.* **2007**, *62* (24), 7505–7514.
- [20] V. van Steijn, C. R. Kleijn, M. T. Kreutzer, *Lab Chip* **2010**, *10* (19), 2513–2518.
- [21] V. van Steijn, C. R. Kleijn, M. T. Kreutzer, *Phys. Rev. Lett.* **2009**, *103*, 21450121.
- [22] T. Taha, Z. F. Cui, *Chem. Eng. Sci.* **2004**, *59* (6), 1181–1190.
- [23] T. Taha, Z. F. Cui, *Chem. Eng. Sci.* **2006**, *61* (2), 665–675.
- [24] N. Shao, W. Salman, A. Gavrilidis, P. Angeli, *Int. J. Heat Fluid Flow* **2008**, *29* (6), 1603–1611.
- [25] D. Y. Qian, A. Lawal, *Chem. Eng. Sci.* **2006**, *61* (23), 7609–7625.
- [26] F. Guo, B. Chen, *Microgravity Sci. Technol.* **2009**, *21*, 51–58.
- [27] L. Dai, W. F. Cai, F. Xin, *Chem. Eng. Technol.* **2009**, *32* (12), 1984–1991.
- [28] S. Rong, B. Chen, *Microgravity Sci. Technol.* **2010**, *22*, 321–327.
- [29] T. T. Fu, Y. G. Ma, D. Funfschilling, C. Y. Zhu, H. Z. Li, *Chem. Eng. Sci.* **2010**, *65* (12), 3739–3748.
- [30] H. Z. Li, Y. Mouline, N. Midoux, *Chem. Eng. Sci.* **2002**, *57* (3), 339–346.
- [31] K. Terasaka, H. Tsuge, *Chem. Eng. Sci.* **1991**, *46* (1), 85–93.
- [32] H. Li, *Chem. Eng. Sci.* **1999**, *54* (13–14), 2247–2254.
- [33] A. Marmur, E. Rubin, *Chem. Eng. Sci.* **1976**, *31* (6), 453–463.
- [34] J. Husny, J. J. Cooper-White, *J. Non-Newton. Fluid* **2006**, *137* (1–3), 121–136.
- [35] R. M. Santos, M. Kawaji, *Int. J. Multiphase Flow* **2010**, *36* (4), 314–323.
- [36] L. D. Youngs, in *Numerical Methods for Fluid Dynamics* (Eds: K. W. Morton, M. J. Baines), Academic Press, London **1982**.
- [37] R. I. Issa, *J. Comput. Phys.* **1985**, *62* (1), 40–65.
- [38] J. U. Brackbill, D. B. Kothe, C. Zemach, *J. Comput. Phys.* **1992**, *100* (2), 335–354.
- [39] Y. P. Hong, H. X. Li, *IEEE Trans. Electron. Packag. Manuf.* **2003**, *26* (4), 273–280.
- [40] C. Cramer, P. Fischer, E. J. Windhab, *Chem. Eng. Sci.* **2004**, *59* (15), 3045–3058.

Research Article: Microbubbles are an important part of chemical and biomedical engineering. Three-dimensional simulations of bubble generation in both Newtonian and non-Newtonian fluids were performed in a microchannel T-junction by the volume-of-fluid model. The influences of viscosity parameter K , power law index n , and yield stress τ_y on the bubble breakup mechanism, shape, size, and generation frequency were investigated.

Three-Dimensional Simulation of Bubble Formation Through a Microchannel T-junction

B. Chen*, F. Guo, G. Li, P. Wang

Chem. Eng. Technol. **2013**, 36 (12), XXX ... XXX

DOI: 10.1002/ceat.201300169

